

## Understanding irradiation damage in high-temperature superconductors for fusion reactors using high resolution X-ray absorption spectroscopy

Rebecca J. Nicholls<sup>1</sup>  <sup>1</sup>✉, Sofia Diaz-Moreno<sup>2</sup>, William Iliffe<sup>1,3</sup>, Yatir Linden<sup>1</sup>, Tayebeh Mousavi<sup>1</sup>, Matteo Aramini<sup>2</sup>, Mohsen Danaie<sup>1</sup> , Chris R. M. Grovenor<sup>1</sup> & Susannah C. Speller<sup>1</sup>  <sup>1</sup>✉

Understanding the effects of fast neutrons on high-temperature superconductors is of growing importance as new compact fusion reactors rely on these materials to generate the high magnetic fields needed to confine the plasma. The critical temperature of the most promising candidate material for small-scale fusion devices, rare-earth barium cuprate, is known to decrease monotonically with radiation dose, indicating the generation of lattice defects everywhere in the material. Here, we use high-energy-resolution X-ray absorption spectroscopy to probe how the local environment around the copper atoms is influenced by point defects induced by  $\text{He}^+$  ion irradiation in the oxygen sublattice. Density functional theory calculations are used to interpret spectral features and we find clear evidence that ion irradiation significantly disrupts the bonding environment around the copper atoms in the copper-oxygen planes responsible for superconductivity in this compound. We propose the generation of a specific Frenkel defect that is consistent with our experimental results. Our results challenge previous assumptions in the literature that irradiation produces point defects only in the chain sites. In addition, we show that partial recovery is possible by annealing at modest temperatures, which may have implications for the operation of superconducting fusion magnets.

<sup>1</sup> Materials Department, University of Oxford, Parks Road, Oxford OX1 3PH, UK. <sup>2</sup> Diamond Light Source, Harwell Science and Innovation Campus, Fermi Ave, Didcot OX11 0DE, UK. <sup>3</sup> Present address: STEP, UK Atomic Energy Authority, Culham Science Centre, Abingdon OX14 3DB, UK.  
✉ email: [rebecca.nicholls@materials.ox.ac.uk](mailto:rebecca.nicholls@materials.ox.ac.uk); [susannah.speller@materials.ox.ac.uk](mailto:susannah.speller@materials.ox.ac.uk)

Nuclear fusion tokamak reactors require high magnetic fields to confine the intensely hot plasma in which the deuterium/tritium reaction takes place. To reduce reactor size and make nuclear fusion more commercially viable, the next generation of small tokamaks currently being developed will rely on deployment of state-of-the-art high temperature superconductors (HTS) to achieve very high magnetic fields in compact windings<sup>1</sup>. The HTS material of choice is  $\text{REBa}_2\text{Cu}_3\text{O}_{7-\delta}$  (RE = rare-earth element), REBCO, which has excellent current carrying capacity at low temperature in extremely high magnetic fields when processed in the form of a  $\sim 1\text{ }\mu\text{m}$  thick pseudo-single-crystal thin film on a flexible metal tape using coated conductor technology<sup>2</sup>.

In operation in a fusion device, the HTS magnet windings will be exposed to a flux of high energy neutrons. Studies on the influence of fission spectrum neutrons and ion irradiation on the superconducting properties of HTS compounds including REBCO, date back to the late 1980s, soon after the discovery of high temperature superconductivity<sup>3–6</sup>. Although interpretation of these results is hampered by inconsistencies in the quality of early single crystal samples, some universal conclusions could be made about the effects of neutron irradiation on the superconducting properties, which have now been confirmed by more recent experiments on coated conductor samples<sup>7–10</sup>. At low neutron fluences, irradiation typically improves the critical current density ( $J_c$ ), except in very low applied magnetic fields that are not very relevant for practical applications. This initial improvement is a result of the generation of additional flux pinning centres. It is followed, at higher fluences, by a severe degradation of the properties and eventually loss of superconductivity associated with the high defect density decreasing the activation energy for flux line motion and hence increasing the flux creep rate<sup>6</sup>. The fluence corresponding to the peak in  $J_c$  depends on various factors including measurement temperature, direction of the applied magnetic field and the pre-existing defect landscape<sup>10</sup>. In contrast, the critical temperature ( $T_c$ ) of the superconductor is found to decrease monotonically with increasing neutron doses up to  $\sim 10^{18}\text{ cm}^{-2}$ , possibly with a plateau at very low doses<sup>6</sup>. Since  $T_c$  measurements are performed at very low currents, this strongly suggests that radiation-induced defects are produced everywhere in the irradiated volume, even at relatively low neutron doses.

Fully oxygenated  $\text{REBa}_2\text{Cu}_3\text{O}_7$  (REBCO) compounds have a complex, layered crystal structure with ordered oxygen vacancies giving rise to two kinds of copper coordination, Cu(1) chains and Cu(2) planes, as shown in Fig. 1a<sup>11</sup>.  $T_c$  is strongly dependent on oxygen stoichiometry. As the O content decreases from 7 towards 6, early polarisation-dependent Cu K-edge X-ray absorption spectroscopy (XAS) studies<sup>12,13</sup> and diffraction studies<sup>14</sup> showed that oxygen atoms are gradually removed from the O(1) site in the chains, resulting in Cu(1) ions becoming 2-fold coordinated with only bonds with the O(4) atoms remaining. This is accompanied by a reduction in the oxidation state of the Cu(1) ions from +2 to +1 and eventually leads to a change in the crystal symmetry from orthorhombic to tetragonal, with even slightly underdoped compounds having drastically reduced  $T_c$  values.

To understand the effects of irradiation on superconducting properties, we need to consider the nature of the defects that are introduced. There is considerable direct evidence from transmission electron microscopy (TEM) that both neutrons and heavy ions produce isolated damage cascades (a few nm in diameter) in HTS cuprates<sup>15–17</sup>. While these TEM-visible features are likely to contribute to the enhanced flux pinning observed at low doses, the presence of isolated damage surrounded by ‘perfect’, undamaged matrix cannot alone explain the observed degradation in  $T_c$  of the bulk material. It is generally assumed,

based on careful annealing experiments, that point defects and small clusters of point defects (mainly in the O sublattice) that cannot easily be observed in the TEM are also produced by neutron irradiation, causing the observed decrease in  $T_c$  and contributing to the initial increase in  $J_c$  by enhancing flux pinning<sup>15,18</sup>.

Light ion irradiation is considered to be a useful proxy for safely investigating the point defect damage generated by neutrons, as well as being useful in its own right as a novel method for ‘writing’ Josephson junction devices in high temperature superconducting thin films by creating local damage using a focused ion beam microscope<sup>19–21</sup>. Irradiation with  $\text{He}^+$  ions<sup>22–25</sup> and protons<sup>26</sup> at energies of 80 keV to 6 MeV have shown that doses of  $10^{14}$ – $10^{16}\text{ cm}^{-2}$  lead to a degradation in  $T_c$  similar to that observed with neutron irradiation, as well as reproducing the peak in  $J_c$ <sup>27,28</sup>. TEM reveals that, even in heavily damaged samples, no nanometre scale cascade damage can be observed<sup>15</sup> although the larger point defect clusters, about 0.3 nm in size, have been observed in proton irradiated samples<sup>27</sup>. Irradiation by light ions in this energy range causes damage mainly by nuclear elastic collisions displacing atoms from their original lattice sites<sup>22,23,26</sup>. The hypothesis that the majority of the radiation damage occurs in the oxygen sublattice is supported by interesting work by Navacerrada et al.<sup>23</sup>. They concluded from X-ray diffraction studies of superlattice structures consisting of YBCO and PrBCO multilayers that the cationic lattice was not disrupted by  $\text{He}^+$  irradiation. Furthermore, Valles et al. speculated that since the chain oxygens are the most weakly bound species in the compound, it is most likely that oxygen atoms are displaced from the O(1) chain sites along the b-axis to the equivalent unoccupied sites along the a-axis<sup>29</sup>. This view was supported by early work by Menushenkov et al.<sup>30</sup> and Navacerrada et al.<sup>23</sup> that found independently from XAS and photo-conductivity measurements, respectively, that  $\text{He}^+$  irradiation produced similar effects to oxygen reduction, and by analogy concluded that irradiation also induces loss of oxygen from the O(1) chain sites. However, transport measurements show that irradiation at moderate fluences leads to the generation of point defects, with the carrier concentration remaining essentially unchanged, suggesting that oxygen is not being completely lost from the REBCO<sup>22</sup>. In contrast to all these previous experiments, Giapintzakis et al. concluded from resistivity experiments on electron irradiated YBCO crystals that displacement of oxygen from the plane sites is responsible for the observed degradation in  $T_c$ <sup>31</sup>, and Zhang et al. also concluded from atomic resolution electron energy loss spectroscopy that heavy ion irradiation creates oxygen vacancies in the planes<sup>32</sup>. Therefore, the hypothesis that it is damage to the oxygen sublattice that is responsible for degradation in  $T_c$  in both light ion and neutron irradiated material is plausible, but the precise nature of the defects is not clear.

XAS is a bulk technique for probing electronic structure and the bonding environment around specific atoms, and therefore it may be a powerful tool for determining the nature of the radiation-induced point defects that are difficult to see in the TEM. The near edge structure of the X-ray absorption spectra (XANES) arises from transitions of core electrons to empty states, and contains information on the oxidation state and local bonding environment (coordination and geometry) of the absorbing atoms. Copper K-edge XAS of YBCO and other cuprate materials has been carried out on early materials from the late 1980s<sup>12,30,33</sup>. The effects of oxygen reduction<sup>12</sup> and  $\text{He}^+$  irradiation<sup>30</sup> have also been studied, with small changes observed in the spectra attributed to changes in the O sublattice. However, as REBCO compounds have two different Cu sites, these early studies were of limited use in identifying the specific defects. In addition to lacking the required energy resolution to clearly

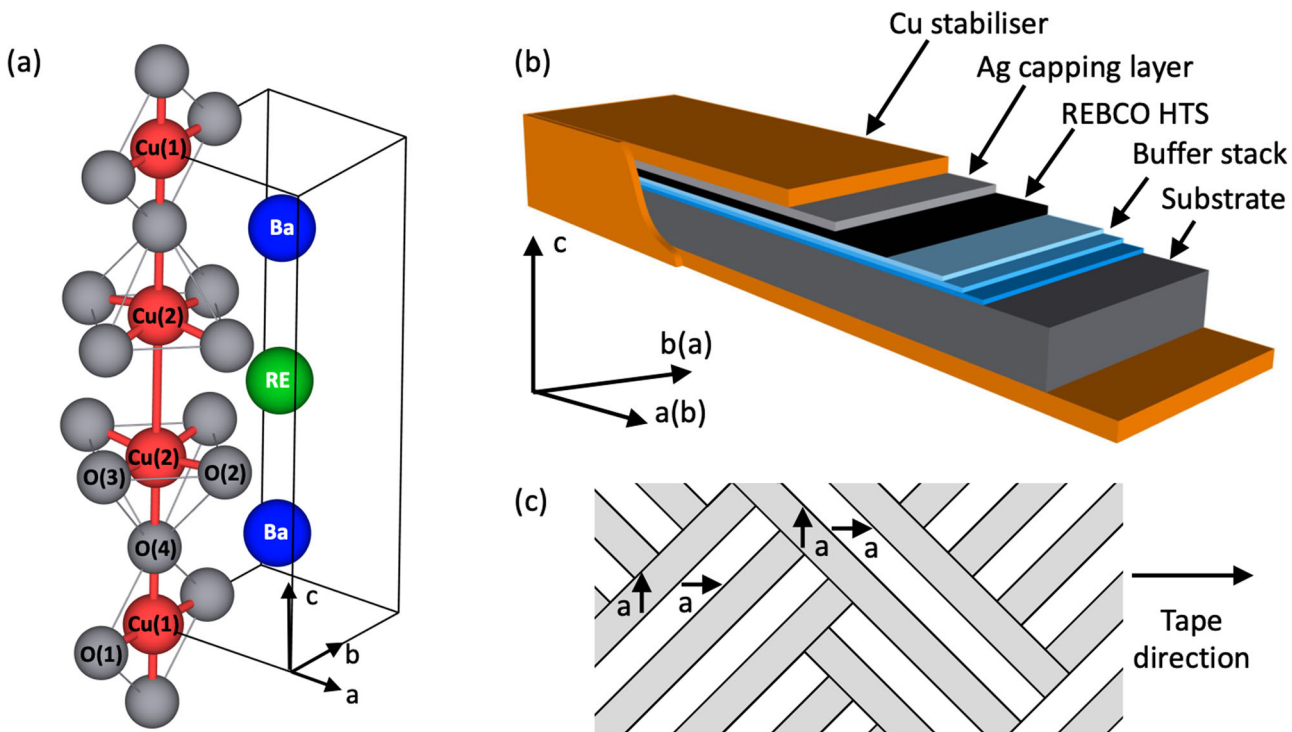


**Fig. 1 Schematic diagrams of a  $\text{REBa}_2\text{Cu}_3\text{O}_{7-\delta}$  (RE = rare-earth element), REBCO, coated conductor. a** Part of the REBCO unit cell showing the two different Cu sites (in red) and their coordination with O atoms (in grey). The Cu(1) chain atoms are 4-fold coordinated in the  $(b,c)$  plane by O(1) and O(4) atoms, whereas the Cu(2) plane atoms are 5-fold coordinated by the O(2) and O(3) atoms in the  $(a,b)$  plane plus the apical O(4) atom. **b** Schematic diagram of a generic coated conductor tape. **c** Schematic diagram of the twin structure with arrows representing the direction of the  $a$ -axis.

distinguish the multiple features in the XANES region, they were generally not supported by computational modelling, instead relying on the ‘fingerprinting’ approach of comparing features in the spectra with similar known compounds. An exception to this is Garg et al., who performed multiple scattering calculations finding qualitative agreement with their experimental data. In addition, they were also able to use the modelling to predict the polarisation dependence of the spectra. For the majority of other papers which did not include modelling, the lack of resolution and inability to distinguish between the different Cu environments led to inconsistencies in the interpretation. For example, the feature following the main absorption peak is interpreted by Antonini et al.<sup>34</sup> to indicate the presence of  $\text{Cu}^{3+}$  in addition to  $\text{Cu}^{2+}$ , by Lytle et al.<sup>35</sup> to arise from Cu(Y) disorder, and by Heald et al.<sup>12</sup> to be the low energy part of the extended X-ray absorption fine structure (EXAFS) region resulting from a higher shell neighbour at around 2.5 Å. The study by Heald et al. on YBCO single crystals is arguably the most illuminating of this early work, as careful analysis of the orientation dependence of the crystal with respect to the polarisation direction allowed indirect conclusions to be made about the assignation of different features in the spectra in the absence of modelling data.

High energy resolution fluorescence detected (HERFD) XAS is a state-of-the-art synchrotron technique that enables absorption spectra to be collected with energy resolution better than the intrinsic broadening determined by the 1s core-hole lifetime, by detecting fluorescent X-rays in a narrow energy range using a crystal analyser<sup>36</sup>. This technique has been successfully applied for studies of 1st row transition metal K-edges, and the L- and M-edges of heavier elements, in a broad variety of scientific disciplines such as chemistry<sup>37–40</sup>, life sciences<sup>41,42</sup> and hard condensed matter<sup>43,44</sup>. Here we report, to the best of our knowledge, the first HERFD-XAS study on a REBCO compound and the only XAS study to date that has been carried out on

technologically important coated conductor samples - the form of the material that will be used to make future fusion magnets - before and after irradiation with  $\text{He}^+$  ions. In addition, density functional theory (DFT) has been used to carefully interpret the spectral features and gain new understanding of the likely irradiation-induced structural defects.

## Results

**Sample properties.** The samples used in this study are 3 mm diameter discs taken from a batch of SuperPower coated conductor, shown schematically in Fig. 1b. The REBCO compound in this tape is  $(\text{Y},\text{Gd})\text{Ba}_2\text{Cu}_3\text{O}_{7-\delta}$  in which the Y is partially substituted for Gd, and 7.5% Zr is added that forms  $\text{BaZrO}_3$  nanorods for improved flux pinning<sup>45</sup>. The REBCO layer is biaxially textured with its  $c$ -axis aligned close to the surface normal, and its  $a/b$  axes aligned along the length of the tape, as shown schematically in Fig. 1b. There is considerable mosaic misalignment (typically up to  $\sim 10^\circ$ ) and the crystals are naturally twinned on the scale of tens of nanometres, with the two twin boundaries along the  $\langle 110 \rangle$  directions and domains rotated by  $90^\circ$  about the  $c$ -axis (Fig. 1c)<sup>46</sup>. Table 1 compares the superconducting properties and structural parameters of the pristine sample with a sample annealed in Ar at  $300^\circ\text{C}$  for 3 h and samples irradiated with 300 keV  $\text{He}^+$  ions to a fluence of  $10^{15}\text{ cm}^{-2}$  and  $10^{16}\text{ cm}^{-2}$ . A post-irradiation oxygen-annealed sample is also included to assess the extent to which irradiation damage can be recovered. The  $T_c$  value is reduced in both the Ar-annealed and He-irradiated samples, with the high fluence of  $10^{16}\text{ ions cm}^{-2}$  suppressing superconductivity entirely. Since only small currents are induced in a  $T_c$  measurement, a drop in the onset temperature of the transition indicates the entirety (bulk) of the material is degraded. The transition also broadens, suggesting an increase in inhomogeneity in Ar-annealed and irradiated samples. X-ray diffraction (XRD) taken in Bragg-Brentano geometry shows a large increase in  $c$ -axis lattice

**Table 1 Summary of the superconducting and structural properties for the samples used in this study.**

Sample	$T_{c,\text{onset}}$ (K)	$\Delta T_c$ (K)	c-axis (Å)	Strain
Pristine	92	8	$11.725 \pm 0.005$	-
Ar-annealed	71	23	$11.740 \pm 0.005$	$0.002 \pm 0.002$
$10^{15}\text{He}^+$	76	20	$11.77 \pm 0.01$	$0.010 \pm 0.005$
$10^{16}\text{He}^+$	<10	-	$11.96 \pm 0.01$	$0.028 \pm 0.005$
$10^{16}\text{He}^+ + \text{O-annealed}$	<10	-	$11.85 \pm 0.01$	$0.011 \pm 0.005$

Superconducting properties have been extracted from magnetisation measurements, further details of which are given in Supplementary Note 1. X-ray diffraction measurements have been used to obtain c-axis lattice parameters and inhomogeneous strain, with the pristine sample used as a strain standard.

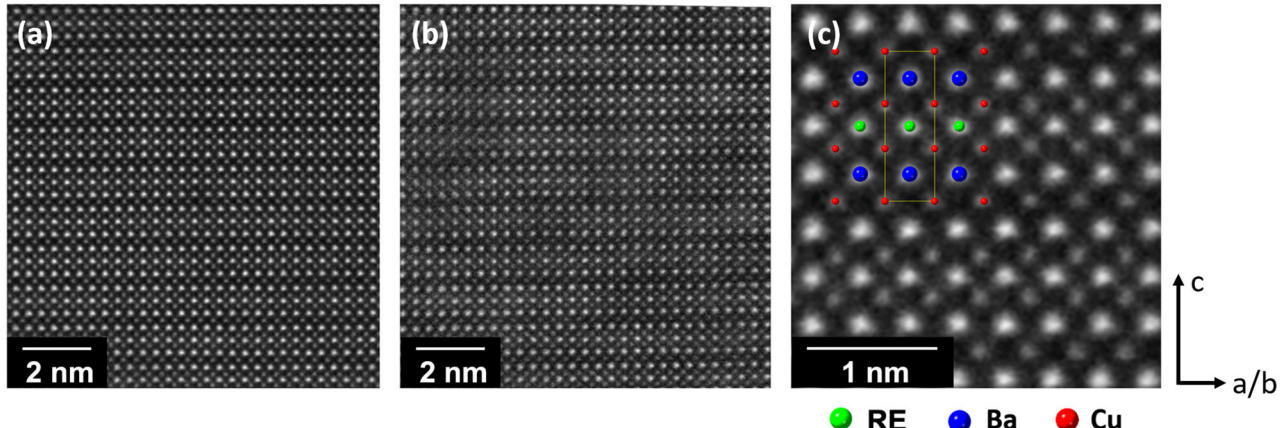


**Fig. 2 Typical examples of aligned stacks of 10 HAADF images. a** HAADF image of the pristine sample. **b** HAADF image of the  $10^{16}\text{ cm}^{-2}\text{ He}^+$ -irradiated sample. **c** Magnified image from a region of **a** with a schematic showing the cation positions in the unit cell.

parameter in the most heavily irradiated sample. Lower dose ion-irradiation and Ar-annealing also increase  $c$  to a lesser extent. This irradiation-induced expansion of the lattice is consistent with previous reports for ion-irradiated and neutron irradiated REBCO,  $\text{MgB}_2$  and A15 superconducting compounds<sup>47,48</sup>. Reducing the oxygen content in REBCO is also well-known to lead to extension of the unit cell in the  $c$ -axis direction<sup>49</sup>, and has led to the assumption that irradiation also leads to O loss. Williamson-Hall analysis of the XRD peak broadening (relative to the pristine sample) shows that considerable inhomogeneous strain is also introduced into the samples as a result of  $\text{He}^+$  irradiation. Oxygen annealing after irradiation with  $10^{16}$  ions  $\text{cm}^{-2}$  results in a slight decrease in  $c$ -axis lattice parameter towards the value of the pristine sample, but the superconducting properties have not been recovered.

**Effect of irradiation on cation lattice.** To explore the effect of  $\text{He}^+$  irradiation on the crystal structure, imaging has been carried out using an aberration-corrected JEOL ARM 300F instrument in scanning transmission electron microscope (STEM) mode at the ePSIC facility. Figure 2a, b show typical high-angle annular dark field (HAADF) lattice images from the pristine and the  $10^{16}\text{ cm}^{-2}\text{ He}^+$  irradiated samples that no longer superconduct. Since HAADF image intensity is mainly dominated by atomic weight, the atomic columns containing heavy RE and Ba atoms appear brightest and the weaker spots are the Cu atom columns, as indicated in Fig. 2c. In this imaging mode the light O atoms contribute little to the intensity of the atomic columns, so point defects on the O sublattice cannot be detected. On inspection of the images from the ion irradiated sample, it is obvious that the cation sublattices are well-preserved; the arrangement of three planes of bright (heavy) Ba-RE-Ba atoms in each unit cell, interspersed with offset Cu planes, apparently remains perfect.

Statistical analysis has been carried out on a number of HAADF STEM images using the Atomap software<sup>50</sup> to fit the positions of the atom columns in a number of aligned image stacks from each sample and extract the lattice parameters, and the results are presented in Fig. 3. Although there is considerable scatter in the data, it can be seen that irradiation generally increases both  $a(b)$ -axis and  $c$ -axis lattice parameters, and for the pristine sample, there appear to be two groups of data points with slightly different  $a/b$ -axis lattice parameters, suggesting that the different twin domains are being sampled. Fewer images were taken from the  $\text{He}^+$  irradiated sample, and it is not clear whether only one type of domain was sampled in this case or whether ion irradiation has reduced the orthorhombic distortion. The absolute values of lattice parameter differ slightly from the reference values and the  $c$ -axis lattice parameters measured by XRD. This is not unexpected as there are likely to be systematic errors from uncertainties in the microscope calibration, scan distortions and random errors introduced by the fitting of the atom column positions. The standard deviation in the calculated lattice parameters within each image is slightly larger in the irradiated samples than in the pristine samples, suggesting that there is more disorder/inhomogeneity in the irradiated sample on the nano scale. This is consistent with the increased inhomogeneous strain observed in the XRD results (Table 1).

These results confirm that the radiation-induced structural changes that are likely to be responsible for the degradation in superconducting properties are caused by changes in the oxygen sublattice, and suggests that, in addition to random disorder that broadens the XRD peaks, there are preferred metastable defect structures where the oxygen atoms are situated at non-equilibrium sites in the structure and result in the measured expansion of the lattice in the  $c$ -direction.

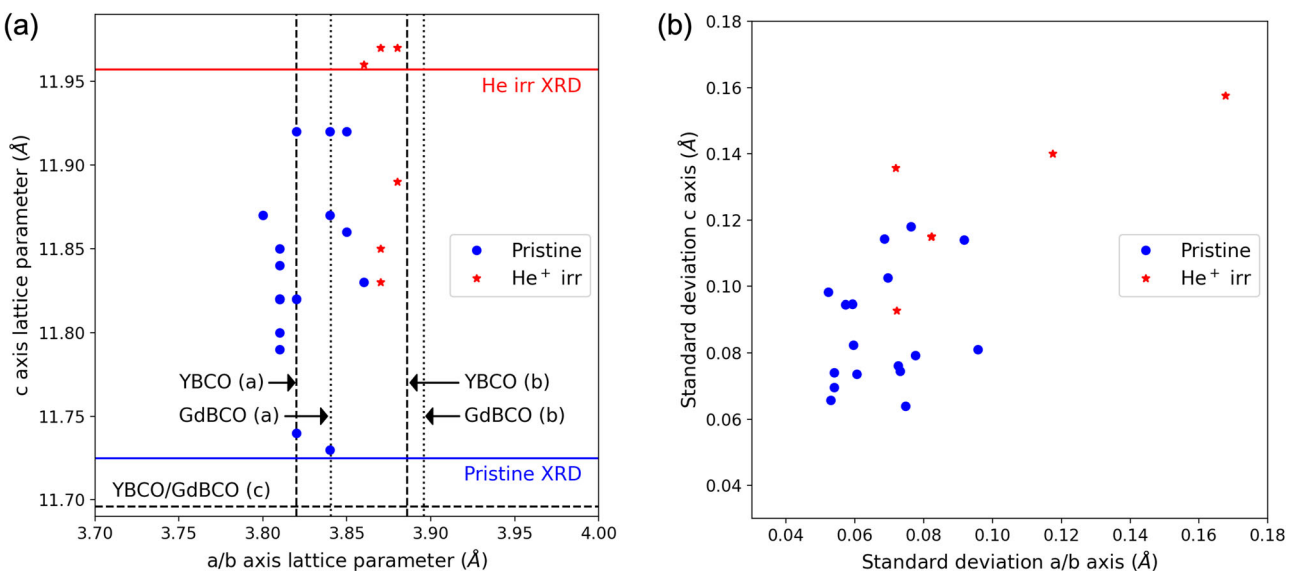


**Fig. 3 Lattice parameter analysis of pristine and  $10^{16}$  He<sup>+</sup> irradiated samples.** **a** Lattice parameter data extracted from aligned stacks of HAADF images such as those shown in Fig. 2. Each data point represents a different image stack, with the lattice parameter values averaged over about 300 unit cells. Reference lattice parameters for YBCO<sup>83</sup> and GdBCO<sup>84</sup> have been added as dashed lines. **b** Standard deviations in lattice parameter for each image.

**Effect of irradiation on the oxygen sublattice.** Copper K-edge HERFD-XAS has been used to examine the effect of irradiation on the local environment of the Cu atoms. As the Cu atoms are surrounded by oxygen nearest neighbour atoms, this approach gives us valuable information about the O sublattice which is invisible in the TEM.

In Fig. 4a, the HERFD-XANES spectra for pristine REBCO coated conductor is compared to the spectra for Cu foil, Cu<sub>2</sub>O powder and CuO powder, standards for Cu in oxidation states 0, +1 and +2, respectively. Since the standards are polycrystalline, they are compared with the REBCO spectrum taken at an intermediate polarisation of 45° to the sample normal. The general shape of the REBCO spectrum most closely resembles the CuO (Cu<sup>2+</sup>) spectrum, with no evidence of the sharp peaks at  $<5$  eV observed in the Cu and Cu<sub>2</sub>O standards. However, there are significant differences between the shapes of the rising edges, with REBCO displaying multiple weak features along the rising edge, whereas CuO has a single strong peak at  $\sim 6$  eV. This has been previously observed by Heald et al. and attributed to either a high degree of covalency or existence of holes in the ligand 2p band<sup>12</sup>.

XAS measurements were obtained at a series of different polarisation directions relative to the crystal lattice of the REBCO by altering the angle of incidence of the linearly polarised x-ray beam. When the incident beam lies at 10° to the sample normal, the polarisation of the electric field was aligned close to the *a/b* directions in the crystal, and at 80° the polarisation was almost aligned with the *c*-axis. Since the XAS experiment probes many twin domains, orientations with an in-plane component of polarisation give an average of the *a* and *b* axis aligned spectra. The polarisation-dependent XANES spectra for the pristine sample in Fig. 4b clearly show systematic variations in the relative intensities of the main features with polarisation angle. The complicated spectra can be split into 3 zones: the pre-edge region (shaded grey), the rising edge (unshaded) and the post-edge region (shaded grey). The rising edge region consists of a series of peaks originating from the dipole-allowed 1s-4p electron transitions. The lowest energy peaks at the start of the rising edge (3–15 eV), are generally considered to originate from 1s-4p transitions accompanied by a shakedown event associated with charge transfer from the ligand<sup>12,51</sup>. These are described

as “well-screened” transitions by Kosugi et al.<sup>52</sup>. The small pre-edge features (<2 eV) originate from weak electric quadrupole transitions from the 1s orbital into the unoccupied 3d orbital, probably with an electric dipole component allowed by hybridisation with p orbitals<sup>51</sup>.

More detailed analysis of the main edge region has been performed by comparing the experimental spectra with spectra simulated from DFT calculations. The YBCO and GdBCO calculated spectra are very similar (see Supplementary Note 3, Supplementary Fig. 3), so for simplicity we will use the YBCO spectra only in the remainder of this paper even though the samples contain both Y and Gd rare-earth elements. The two extremes of orientation, 80° (with  $\hat{E}$  aligned close to the *c*-axis) and 10° (with  $\hat{E}$  aligned close to the *a/b* axes), are shown in Fig. 4c, d. The modelled contributions from the Cu(1) and Cu(2) sites are displayed separately, along with the sum spectrum (weighted in the ratio 1:2 to account for there being twice as many Cu(2) sites as Cu(1) sites in the crystal structure). In the  $\hat{E} \parallel a/b$  case, the modelled spectra with polarisation parallel to *a* and *b* are shown separately, and the total model uses the average of the two to replicate the experiment where both twin domains are sampled. In the 80° spectrum, there are four distinct features associated with the main edge, labelled A, B, C and D. Features A-C clearly correspond to peaks in the Cu(2) model, whilst peak D matches the main peak in the Cu(1) model. Similar features were observed in the previous polarisation-dependent XAS study by Heald et al.<sup>12</sup>. Using simple molecular orbital considerations that take into account only nearest neighbour Cu-O bonds, we would expect to see a pair of Cu(2) peaks relating to well-screened and poorly screened transitions to Cu(2) 4p $\pi$  orbitals. However, our modelling shows the presence of three distinct Cu(2) peaks, with a clear shoulder on the low energy side of the peak at C, that match closely with experiment. Visualisations of the charge density (see Supplementary Note 3, Supplementary Fig. 4) suggest the bands responsible for these features along the rising edge are not simple nearest neighbour molecular orbitals with the O(2)/O(3) atoms in the Cu(2) plane, but with considerable involvement of the RE, Ba, other Cu atoms and the O(4) apical atom. Peak D originates from the Cu(1) spectrum and charge density visualisations (see Supplementary Note 3,

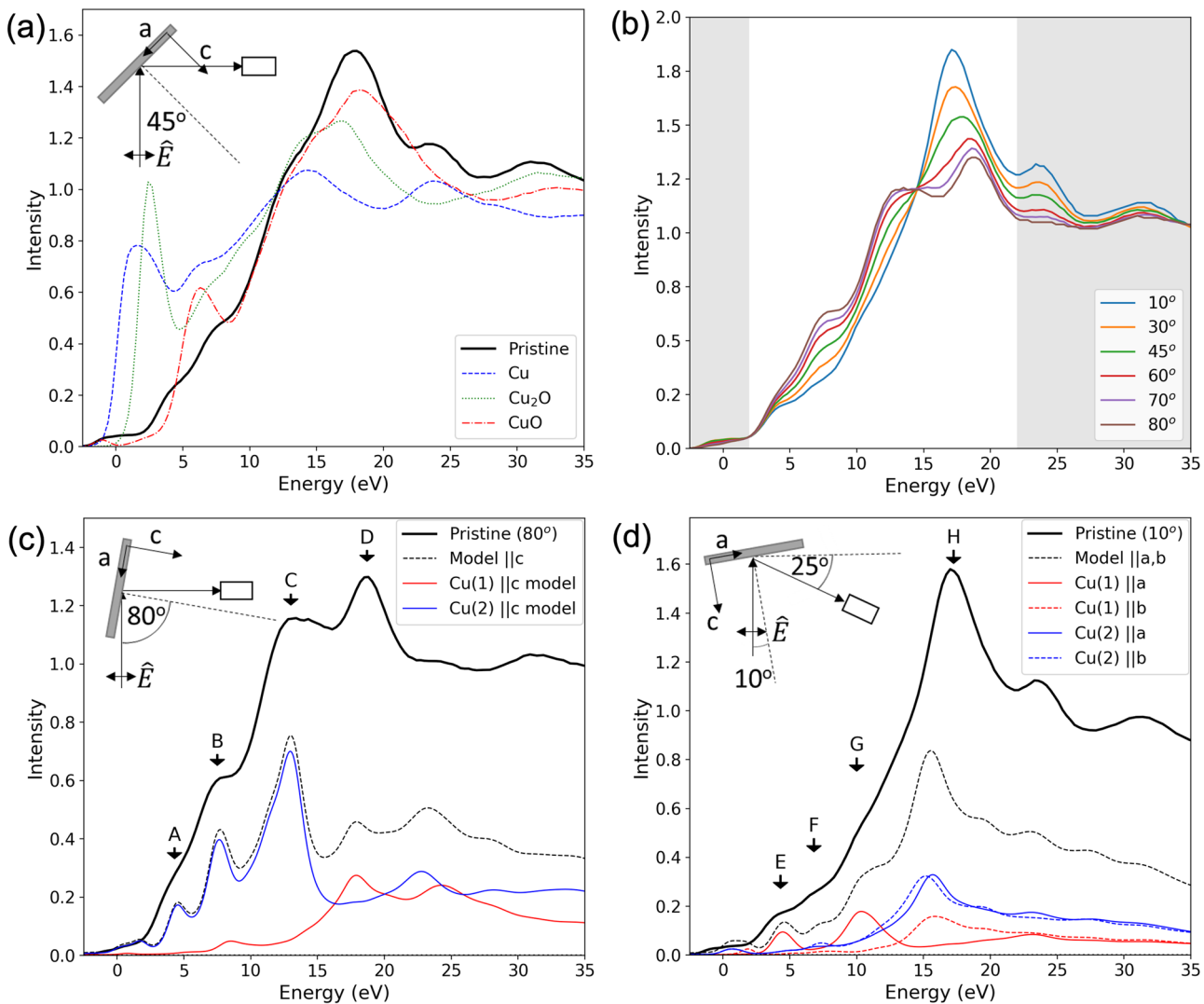


**Fig. 4 Cu K-edge XANES spectra for pristine samples.** **a** Comparison of XANES spectra taken from the pristine REBCO coated conductor with polycrystalline Cu foil, Cu<sub>2</sub>O powder and CuO powder standards. All data taken with the incident beam at 45° to the sample normal. Following the method in Heald et al.<sup>12</sup>, the energy calibration has been performed by setting zero energy to the first peak in the first derivative of the spectrum from the Cu foil standard. **b** Orientation-dependent XANES spectra for the pristine REBCO sample. Comparisons of the 80° and 10° experimental data from the pristine sample with  $\hat{E}||c$  and  $\hat{E}||a/b$  modelled spectra calculated by DFT are shown in **c** and **d**, respectively. Insets show schematic diagrams of the experimental geometry.

Supplementary Fig. 5) confirm it to be a transition to the Cu(1)-4p $\sigma$  orbital with the O(4) atom, consistent with the analysis of Heald et al.<sup>12</sup>.

XANES spectra taken with the polarisation aligned close to the *a/b* axes (Fig. 4d) also exhibit 4 distinct features, but the shape of the spectrum is very different from the  $\hat{E}||c$  spectrum. Two peaks on the rising edge (E and G) correspond to Cu(1) transitions, whereas the main peak H and the weak feature F correspond mainly to Cu(2) transitions. Understanding the origin of these features is more complex in this orientation as the nanoscale twinning means that the experimental spectra have contributions from two symmetrically non-equivalent cases:  $\hat{E}||a$  and  $\hat{E}||b$ . As discussed extensively by Heald et al., Cu(2) 1s-4p transitions are expected in both domains as there are Cu(2)-O $\sigma$  bonds with O(2) atoms along the *a* direction and with O(3) atoms in the *b* direction. However, for domains where  $\hat{E}||a$ , a peak corresponding to the Cu(1) 1s-4p $_{x\pi}$  transition should also be observed as the Cu(1)-O bonds are arranged in the (*b,c*) plane, whereas for  $\hat{E}||b$  the Cu(1) 1s-4p $_{\sigma}$  transition originating from the Cu(1)-O(1)

bonds aligned along the *b*-axis should be observed. Comparing this molecular orbital picture with the results of our DFT modelling, the features on the rising edge at E and G can clearly be seen to correspond to peaks in the Cu(1)  $\hat{E}||a$  modelled spectrum. Charge density visualisations (see Supplementary Note 3, Supplementary Fig. 6) clearly show that the peak at E can be attributed to a Cu(1) 4p $_{x\sigma}$  orbital with the Cu(1) atom in the adjacent unit cell which is not picked up in the molecular orbital picture. The peak at G is more difficult to interpret from the charge visualisations, but there is some indication that it arises from transitions into a Cu(1) 4p $_{x\pi}$  orbital formed with the O(4) atom, which are expected from the molecular orbital picture. Peak H is seen to mainly arise from the Cu(2) 4p $_{x\sigma}$  transitions, with a smaller contribution from the weaker Cu(1) 4p $_{y\sigma}$  transition which occurs at a similar energy. The weak feature F at an energy of ~6.6 eV mainly corresponds to a small peak in the Cu(2)||b spectrum which also arises from 4p $_{y\sigma}$  transitions. However, in this case there appear to be additional interactions with the apical O(4) atoms.

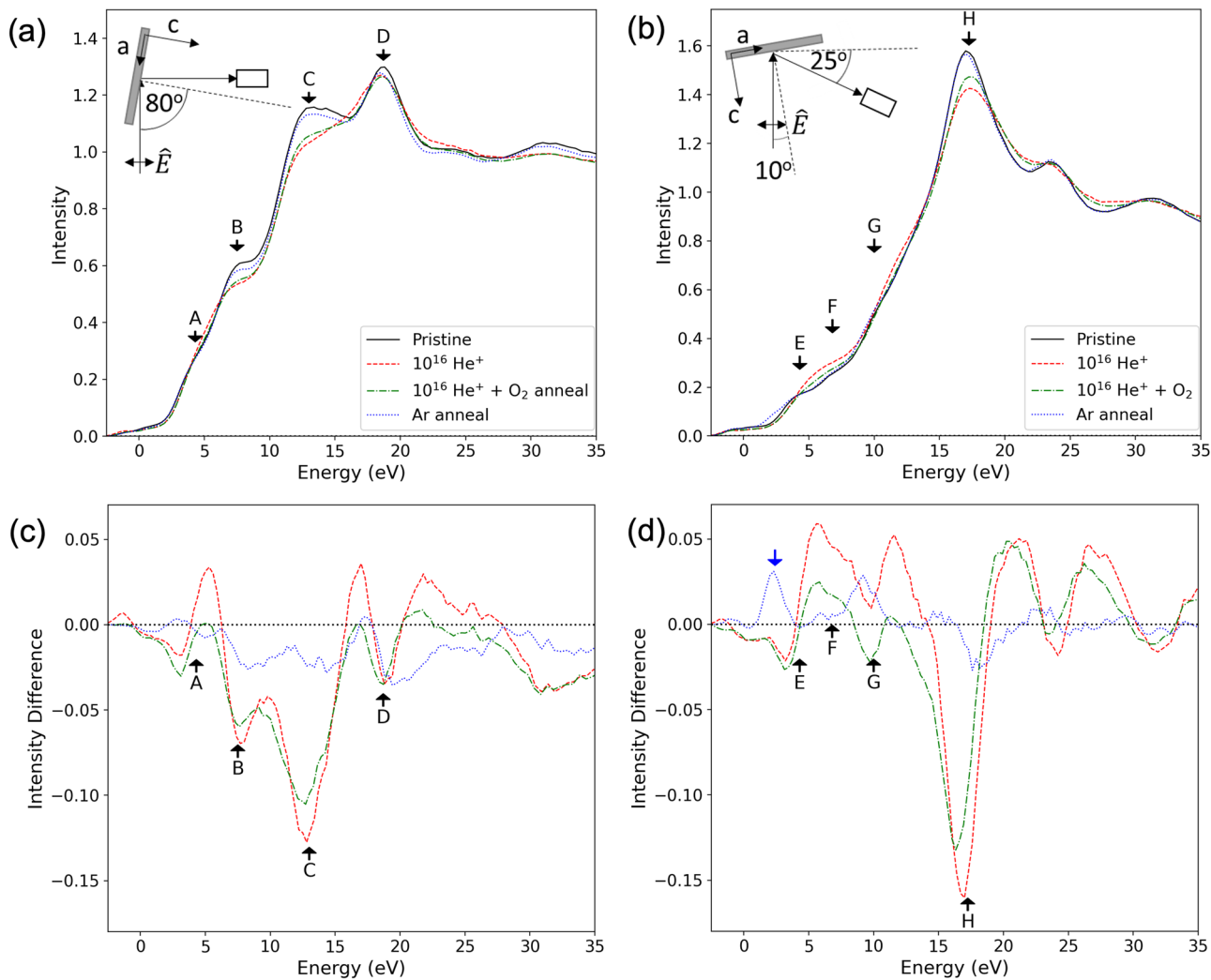


**Fig. 5 Comparison of XANES spectra for pristine, Ar-annealed, He<sup>+</sup>-irradiated and post-irradiation oxygen-annealed coated conductor samples.**

**a, b** Show spectra for angles of incidence of 80° ( $\hat{E}||c$ ) and 10° ( $\hat{E}||a/b$ ), respectively. **c, d** Give the corresponding difference spectra, relative to the pristine sample. An additional peak in the  $\hat{E}||a/b$  spectrum of the Ar-annealed sample is indicated with a blue arrow.

As mentioned in the Introduction, Garg et al. used multiple scattering calculations to predict the orientation dependence of YBCO<sup>53</sup>. They calculated the features on the rising edge for  $\hat{E}||c$  would come from the Cu(2) atoms and would come from the Cu(1) atoms in the  $\hat{E}||a,b$  case, which is what we have found, but the shape of the edge is only qualitatively similar. More sophisticated multiple scattering calculations agree well with our DFT calculations (see Supplementary Note 4).

Figure 5 compares the 80° and 10° spectra of samples that have undergone different treatments. The sample annealed in Ar for 3 h and the sample He irradiated to a dose of  $10^{15}$  ions  $\text{cm}^{-2}$  (not shown) are very similar to the pristine (untreated) sample. However, irradiating with He<sup>+</sup> to the higher dose of  $10^{16}$  ions  $\text{cm}^{-2}$  results in dramatic changes to the absorption spectra. Most significantly, it can be seen by inspection of the XANES spectra that most of the peaks originating from Cu(2) transitions (B, C and H) are seen to decrease in intensity, whereas the main peaks from the Cu(1) transitions (D and G) are hardly affected. This strongly suggests that He<sup>+</sup> irradiation affects the Cu(2) ions and their local environment. It is also interesting to note the considerable enhancement in spectral weight in a broad region of the  $\hat{E}||a/b$  spectrum around feature F in the 5–8 eV range for the  $10^{16}$   $\text{cm}^{-2}$  He<sup>+</sup> irradiated sample. Slight enhancement is also seen between peaks A and B in the  $\hat{E}||c$

spectrum and the main peak at D is considerably broadened. These broad features may indicate an increase in the structural disorder in the samples which is consistent with the increased inhomogeneous strain measured by XRD (see Table 1). Oxygen annealing of the  $10^{16}$   $\text{cm}^{-2}$  He<sup>+</sup> irradiated sample leads to a slight return towards the shape of the pristine spectra, indicating that at least some of the radiation-induced structural defects can be annealed out.

Many previous XAS and XRD experiments have shown that annealing in inert or reducing environments initially removes oxygen from the Cu(1) chains, leaving the Cu(1) ions 2-fold coordinated along the *c*-axis direction<sup>14</sup>. This is accompanied by the Cu(1) ions becoming reduced from the 2+ to the 1+ oxidation state. The difference spectra shown in Fig. 5d reveal the appearance of a small additional peak in the Ar-annealed sample 10° spectrum at ~2 eV, highlighted by an arrow. This corresponds well to a peak in the experimental Cu<sub>2</sub>O spectrum shown in Fig. 4b and is consistent with other studies on 2-fold co-ordinated Cu<sup>1+</sup> compounds<sup>51</sup>. Although this strongly suggests the presence of Cu<sup>1+</sup> ions in the Ar-annealed sample, Kosugi et al. warn against using this feature as a definite signature of the +1 oxidation state because changes in the local bonding geometry also strongly influence the edge structure<sup>52</sup>. However, the absence of this feature in the He<sup>+</sup> irradiated samples is a good indication

that different mechanisms are responsible for reduction in the superconducting transition temperature in  $\text{He}^+$  irradiated and Ar-annealed samples.

**DFT modelling of defect structures.** To shed light on the origin of the radiation-induced structural changes in the absorption spectra, various specific oxygen defects were explored using DFT modelling. Table 2 shows the result of geometry optimisations on structures containing a variety of different defects: a vacancy on the O(2) site in the Cu(2)-O plane, an oxygen interstitial half-way between the Cu(2) and Cu(3) atoms in the RE plane at position (0,0,0.5) in the unit cell (hereafter referred to as site I), and the combined Frenkel defect formed by moving oxygen from O(2) to the interstitial site I (shown in Fig. 6a). Structures with vacancies on the O(1) and O(4) sites in the chain are also included for comparison. It can be seen that, with the exception of the O(1)

vacancy that removes the orthorhombic distortion, these defects have minimal effect on the  $a/b$  lattice parameters. However, introduction of oxygen at interstitial site I (either on its own or in the Frenkel defect) results in a considerable increase in the  $c$ -axis lattice parameter. This is consistent with the XRD results presented in Table 1 that show irradiation causes an expansion of the unit cell in the  $c$  direction. (It is noted that it was not possible to measure  $a/b$ -axis lattice parameters using XRD in the  $\theta - 2\theta$  geometry owing to the strong biaxial texture of the samples).

It is well-known from previous experiments by many researchers that the  $c$ -axis lattice parameter also increases with decreasing oxygen stoichiometry, as O atoms are gradually removed from the O(1) site in YBCO<sup>49</sup>, increasing from about 11.66 Å to about 11.82 Å as the oxygen stoichiometry changes from 7 to 6. There is a similar (but slightly weaker) trend for GdBCO. However, our geometry optimisations of the O(1) vacancy structure do not result in a significant increase in the  $c$ -axis lattice parameter, nor can we find other modelling studies where O(1) vacancies alone produce this expansion. Therefore, we conclude that loss of oxygen from the copper-oxygen chains cannot by itself explain the very large increase in lattice parameter in the heavily ion-irradiated samples to about 11.96 Å, or even the smaller expansion after Ar-annealing (to 11.74 Å). However, our DFT modelling suggests that the introduction of even a dilute concentration of interstitial oxygen at site I between the Cu-O planes could account for the increase  $c$ -axis lattice parameter (see Supplementary Note 5, Supplementary Table 1).

Unlike Ar-annealing where we expect loss of oxygen from the material, the  $\text{He}^+$  irradiation process is more likely to displace oxygen atoms rather than remove them from the material entirely. Therefore, to investigate the spectral changes observed

**Table 2 Lattice parameters for various oxygen defect structures calculated by geometry optimisation of the unit cell.**

Structure	$a$ (Å)	$b$ (Å)	$c$ (Å)
ICSD (Collection code 44116) <sup>83</sup>	3.82	3.89	11.68
Pristine	3.82	3.88	11.66
Interstitial O at site I	3.83	3.88	12.17
Vacancy at O(2) site	3.82	3.88	11.68
Frenkel defect O(2) $\rightarrow$ (0,0,0.5)	3.82	3.89	12.23
Vacancy at O(1) site	3.84	3.84	11.67
Vacancy at O(4) site	3.84	3.89	11.67

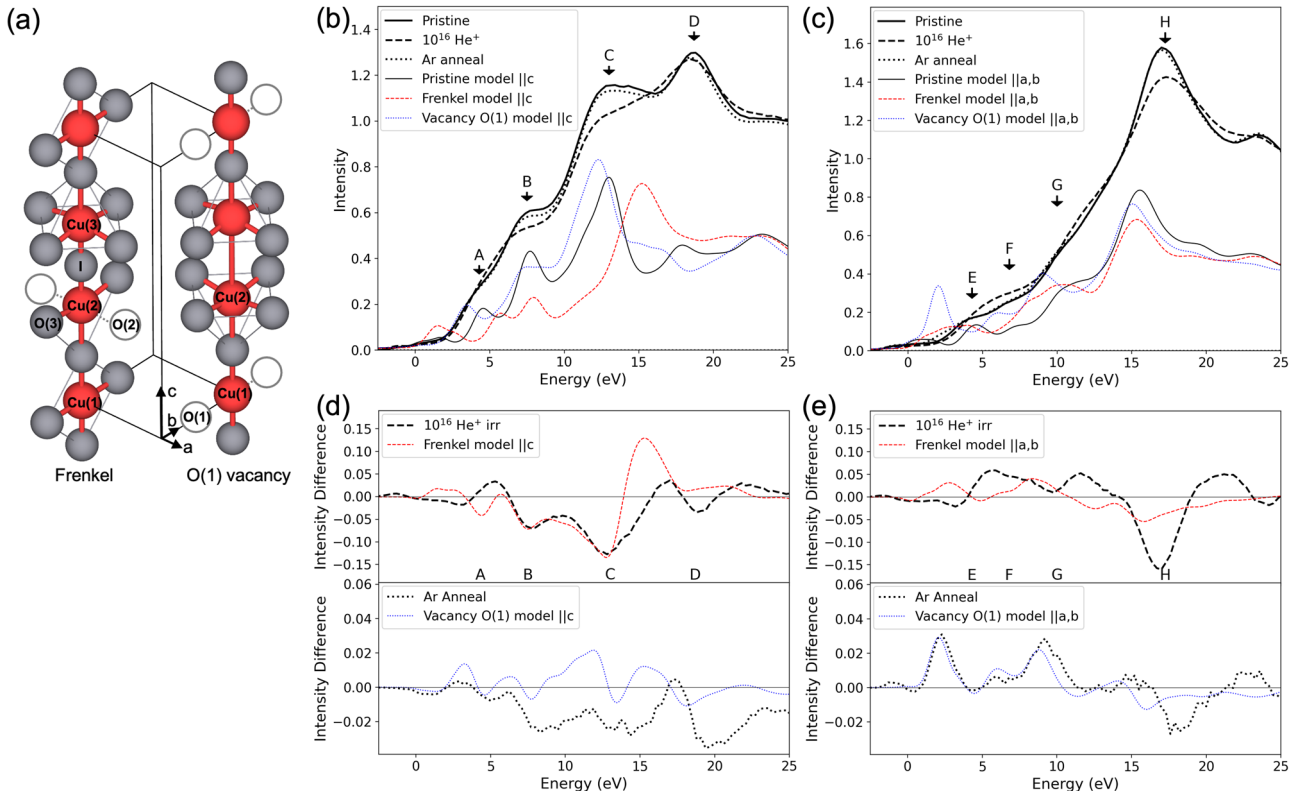


**Fig. 6 Comparison of XANES spectra with DFT calculated spectra from selected defect models.** **a** Schematic diagrams showing the Frenkel and O(1) vacancy defects. Comparison of the pristine,  $10^{16} \text{ He}^+$  irradiated and Ar annealed samples with the pristine, Frenkel and O(1) vacancy defect models for YBCO, for **b**  $\hat{E}||c$  and **c**  $\hat{E}||a/b$  with the  $\hat{E}||a/b$  modelled spectra being the average of the  $a$  and  $b$  spectra. **d, e** Show the corresponding difference spectra with the experimental  $\text{He}^+$  irradiated and Ar annealed spectra shown relative to the experimental pristine spectra, and the Frenkel and O(1) vacancy models shown relative to the pristine model.

on irradiation, we have initially chosen to compare the data with spectra simulated from the Frenkel defect model that both reproduces the experimental increase in *c*-axis lattice parameter and conserves oxygen atoms. Figure 6 compares the experimental XANES spectra measured from the pristine and  $10^{16} \text{ cm}^{-2}$   $\text{He}^+$  irradiated samples with the spectra calculated from the pristine and Frenkel defect models of YBCO. Firstly, we will examine the spectral changes in the  $\hat{E}||c$  spectra shown in Fig. 6b, that are more clearly visible in the difference spectra in Fig. 6d. The most striking irradiation-induced spectral changes are the decrease in intensity of the features at B and C, along with the change in shape of spectrum in the region between C and D. The Frenkel defect model reproduces the reduced intensity at B and C, and the apparent shift in the peak at C to higher energies. In addition, the small peak at A appears to have shifted to higher energies in the Frenkel defect model, which may account for the increase in spectral weight observed between A and B in the irradiated sample. The O(1) vacancy model, also shown in Fig. 6, does not reproduce the spectral changes that happen as a result of irradiation. However, Fig. 6d shows it matches well with the spectral changes that occur when the sample is Ar-annealed.

Figure 6c shows the average of the spectra parallel to the *a* and *b* axes calculated from the pristine and Frenkel defect models (the individual  $||a$  and  $||b$  spectra are shown in Supplementary Note 5). Although the energies do not match up exactly, the decrease in intensity of peak H, which is the most striking difference between the irradiated and pristine experimental spectra, is reproduced by introducing Frenkel defects. The irradiated spectrum also shows slight increase in spectral weight in a broad range between peaks E and F and just after peak G. Although the Frenkel defect model does show increased spectral weight around F, the difference spectra in Fig. 6e reveal that the match with experiment is not very close. In addition the experimental increase in spectral weight above G is not reproduced by the Frenkel defect model. This is not surprising, since we have shown that the features at E and G in the pristine model originate from the Cu(1) chain site so we would not expect them to be affected by the specific Frenkel defect that we have studied here. However, the O(1) vacancy model does not reproduce the observed spectral changes on irradiation any better than the Frenkel model, and the characteristic peak at about 2 eV in the O(1) vacancy model is not present in the spectrum from the irradiated sample. In contrast, the O(1) vacancy model is an excellent match to the Ar-annealed sample, as can clearly be seen in the difference spectra in Fig. 6e.

The Frenkel defect model we have considered has thus reproduced many, but not all of the spectral changes we see in the irradiated samples. In this model, all of the O(2) atoms have been moved to the interstitial position, whereas, in reality, we would expect only some of the O(2) atoms to be displaced. This is evidenced by the *c*-axis parameter increase being overestimated by the model. So far we have also only considered the situation where all interstitial atoms have originated from O(2) sites, which may not be the case. Therefore, we now consider how the Frenkel defect spectra are related to the spectra from O(2) vacancies and interstitial oxygen separately. Figure 7a, b show that the Frenkel defect spectra are not simply a linear sum of the spectra simulated from O(2) vacancies and interstitial defects, demonstrating that interaction between the constituent defects plays a role in the resulting spectra. However, some of the features in the Frenkel model can be attributed to either O(2) vacancies or interstitials. For example, in the  $\hat{E}||c$  case the reduction in spectral weight between B and C is a result of the interstitial and the majority of changes in the  $\hat{E}||a/b$  spectra result from the vacancies. The experimentally observed shift in spectral weight to slightly higher

energy between B and C on irradiation is only reproduced by the presence of the interstitial. However, from the defects we have studied, the increase in intensity between E and G cannot be explained by the interstitial alone, requiring the presence of either O(2) or O(1) vacancies.

Given that previous studies have suggested that the reduction in  $T_c$  upon irradiation may be a result of the introduction of O(1) vacancies, we have explored the possibility that Frenkel defects and O(1) vacancies are both present in the irradiated material by performing a linear combination of the simulated spectra from both defects (see Supplementary Note 5, Supplementary Fig. 12). The combined spectra do not improve the agreement with the experimental data. However as this is a linear combination, and we have seen that defects do interact, this may not be fully representative of the presence of both defects. We do not find any evidence that  $\text{He}^+$  ion irradiation removes oxygen atoms from the O(1) chain site completely, but we have not ruled out that the chains may become disordered by some O(1) atoms migrating to the unoccupied equivalent site along the *a*-axis. We would not expect to see significant spectral changes as a result of this kind of disorder, were it present, because the samples we have studied are twinned and we are measuring an average of the contributions from  $\hat{E}||a$  and  $\hat{E}||b$ .

In addition, we have not explored the possibility that the O(4) atoms may have been displaced. However, studies by Benzi et al. have ruled out the presence of O(4) vacancies in low oxygen content YBCO samples and our DFT geometry optimisations show that O(4) vacancies by themselves do not increase the *c*-axis lattice parameter significantly. In agreement with previous work, our calculations also indicate that O(4) vacancies are not as low in energy as O(1) vacancies.

As a comparison to ion irradiation, the XANES results on samples that have been annealed in a reducing Ar atmosphere are also included in Fig. 6. Both treatments lead to a decrease in  $T_c$  and an expansion in *c*-axis lattice parameter, but the spectral changes are quite different. In particular, reduction of the REBCO is characterised by the appearance of a new peak at around 2 eV in the  $\hat{E}||a/b$  spectrum shown in Fig. 6. This suggests the presence of Cu in the +1 oxidation state because it closely matches the position of the peak in the  $\text{Cu}_2\text{O}$  standard sample (Fig. 4a). This peak is also reproduced in our O(1) vacancy model, providing strong evidence supporting the previous diffraction experiments that oxygen is preferentially lost from the O(1) chain sites in oxygen-deficient samples<sup>12–14</sup>. However, it is interesting to note that despite the close match with the experimental XANES spectra, our DFT calculations do not reproduce the modest *c*-axis lattice expansion that occurs as a result of Ar-annealing just by removal of O(1) atoms. Given that the only oxygen defect that we have found to increase the *c*-axis lattice parameter is oxygen at the interstitial site I, we speculate that Ar-annealing removes oxygen preferentially from the O(1) sites, but that some displaced oxygen atoms may remain in the lattice in the interstitial site. To investigate this hypothesis, DFT calculations have been carried out in which all of the O(1) atoms have been removed and either a quarter or a half of the interstitial sites have been filled with an oxygen atom. For the case where a quarter of the interstitial sites were filled, the *c*-axis parameter was found to increase to 11.70 Å and when half of the sites were filled it increased to 11.85 Å, values well within the range measured experimentally. In addition, when the modelled spectra from the O(1) vacancy is combined with that from the interstitial (see Supplementary Note 5, Supplementary Fig. 13), the simulated spectrum is still compatible with the experimental data for the Ar annealed sample. Although this analysis suggests that our experimental data are consistent with the possibility that some oxygen atoms

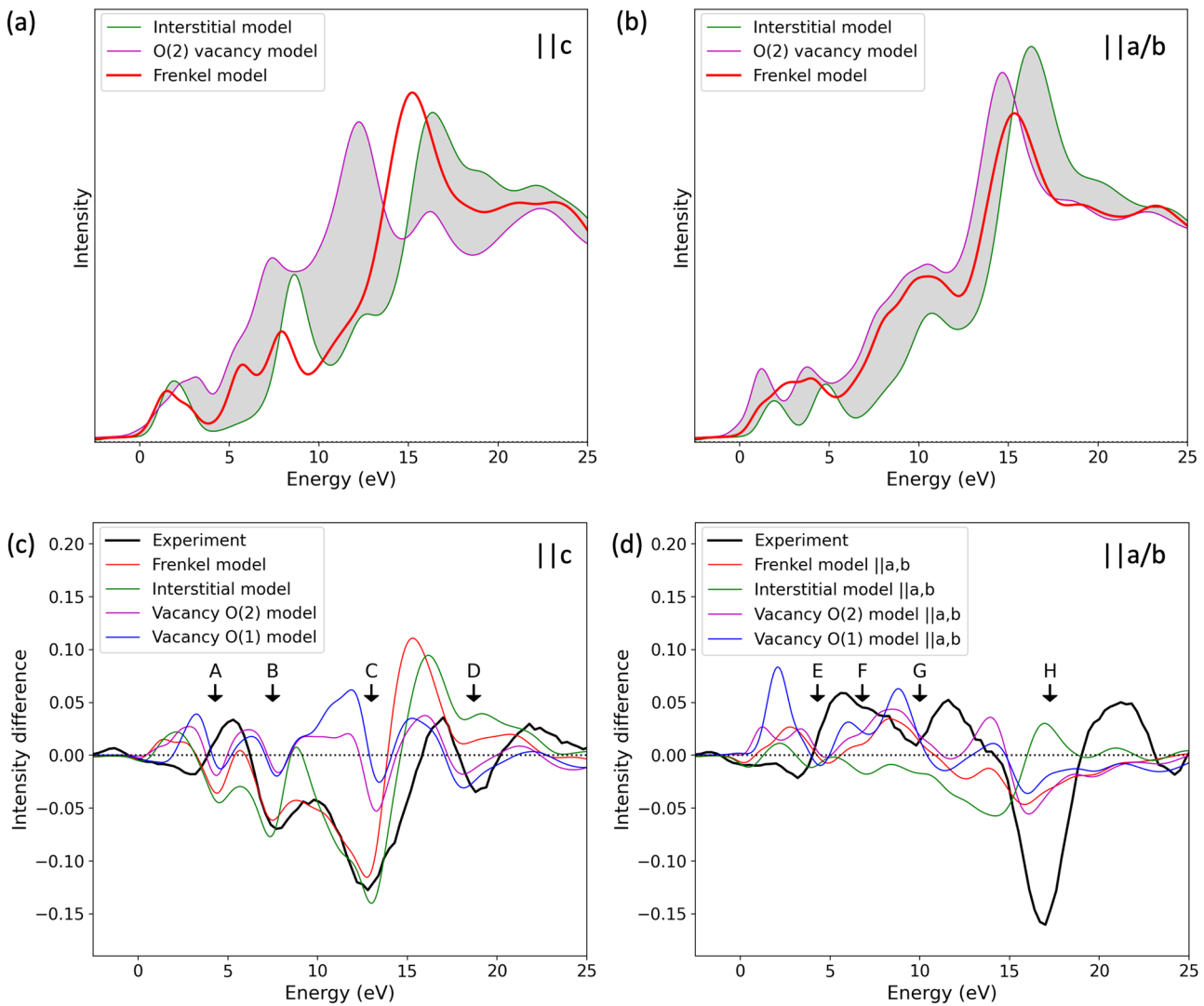


**Fig. 7 Comparison of the Frenkel defect model with the constituent interstitial and vacancy defect models.** **a, b** Comparison of linear combinations of spectra simulated from interstitial oxygen at site I and O(2) vacancy models with the Frenkel defect model  $\hat{E}||c$  and  $\hat{E}||a/b$ , respectively. **c, d** Difference spectra comparing  $10^{16}$   $\text{He}^+$  ions  $\text{cm}^{-2}$  irradiated relative to pristine experimental data with various defect models compared with the pristine model, for  $\hat{E}||c$  and  $\hat{E}||a/b$ , respectively.

become trapped in the interstitial site, it does not provide conclusive evidence, nor does it preclude oxygen being displaced to other sites in the lattice.

The conclusion of this detailed analysis is that irradiation-induced defects are different to the ones induced by simple reduction using an Ar-anneal. The spectral changes produced by irradiation with  $\text{He}^+$  ions can largely be explained by Frenkel defects consisting of oxygen interstitials at site I and oxygen vacancies in the Cu(2) plane. There is no evidence that  $\text{He}^+$  irradiation leads to the removal of oxygen from the O(1) chain sites, resulting in the Cu(1) atoms being 2-fold coordinated, as clearly occurs in the Ar-annealed samples. However, our analysis has not ruled out the presence of oxygen disorder in the Cu(1) plane between the O(1) sites and the equivalent sites along the  $a$ -axis, which we do not expect to lead to significant spectral changes owing to the presence of [100]/[010] twins in the sample.

## Discussion

Radiation damage, particularly in metals, has been studied extensively both experimentally<sup>54</sup> and theoretically<sup>55</sup>. In general,

when high energy ions or neutrons collide with atoms in a crystalline material, atoms in the target absorb energy from the projectile atom, and become displaced from their equilibrium sites. Subsequently these primary knock-on atoms (PKAs) collide with surrounding atoms, generating further displacements. Thermally activated relaxation of this damaged structure allows the lattice to return towards a stable arrangement, but high concentrations of lattice defects such as vacancies and interstitials remain which can diffuse through the lattice and mutually annihilate or cluster.

Previous work on the radiation damage of REBCO, reviewed in the Introduction, has concluded that defects in the oxygen sub-lattice are mainly responsible for the observed decrease in the superconducting transition temperature<sup>56</sup>. Several groups have reported the likelihood that most of the defects involve the migration of oxygen atoms from the chain sites based on indirect evidence from comparing experimental results from irradiated samples with reduced samples. However, our XANES analysis reveals significant differences between  $\text{He}^+$  ion irradiation and simple Ar-annealing to remove oxygen, and clearly indicates that the oxygen atoms in the Cu planes are also affected by ion irradiation.

The possibility of irradiation causing considerable disorder in oxygen ions in both plane and chain sites, rather than just the chain sites, is perhaps not surprising. Stoneham and Smith concluded from reviewing the early irradiation studies on high temperature superconducting cuprates that defects are created on all of the sublattices, but there is a greater extent of recovery on the cation sublattices. Our simple transport of ions in matter (TRIM) analysis of the irradiation of YBCO by  $10^{16}$  ions  $\text{cm}^{-2}$  of 300 keV  $\text{He}^+$  predicts, using standard displacement energies of 25 eV for Y, Ba and O and 40 eV for Cu<sup>57</sup>, that there will be about 10% vacancies on each of the different sites, which is consistent with Stoneham and Smith's 'shake it all up' description. However, there is general agreement in the literature that the O atoms are bound more weakly in the chain sites, which has not been taken into account in the simple TRIM analysis. The displacement threshold energy of chain oxygens is found to vary wildly, with many reporting typical values of around 20 eV<sup>31,56</sup>, although values as low as 10 eV and 2 eV have also been reported<sup>58,59</sup>. The plane oxygen displacement energy is less clear, with Tolpygo et al. finding values of about 8 eV<sup>59</sup>, but Giapintzakis putting an upper limit of around 64 eV<sup>31</sup>. The same study gives a value of 25 eV for the displacement energy of Cu atoms. The lower displacement energy for chain oxygens relative to plane oxygens is also consistent with theoretical calculations of desorption energies<sup>60</sup> and vacancy formation energies<sup>61,62</sup>. In addition, molecular dynamic simulations by Gray<sup>63</sup> show that the threshold displacement energies are very angle-dependent, with typical values for oxygen of 9–26 eV, although in some directions displacement energies as low as 2.5 eV or as high as 64 eV have been found. Their molecular dynamics (MD) simulations of low energy (5 keV) impacts show that more oxygen vacancies are created than cation vacancies, reflecting the lower threshold displacement energies of this sublattice, and that after the initial impact there is less recombination of oxygen defects compared to the other cation defects. Despite this complexity and uncertainty in suitable threshold displacement energies, since our basic TRIM analysis uses threshold energies near the upper end of those reported in the literature, it is reasonable to assume that 300 keV  $\text{He}^+$  ions will have sufficient energy to displace plane site oxygen ions as well as those occupying chain sites.

Both the XRD and the XANES results presented here show that it is possible to reduce the structural damage caused by a high dose of  $\text{He}^+$  irradiation by annealing in oxygen, although superconductivity in this highly damaged sample has not returned. Oxygen is highly mobile in the REBCO structure<sup>60</sup>, so it is not surprising that the concentration of defects on the oxygen sublattice decreases on annealing, especially if displaced oxygen is not removed from the sample. Considerable recovery has also been reported previously in samples that have been irradiated to a lesser extent using neutrons, protons and electrons<sup>15</sup>, and a recent paper by Iliffe et al. shows that the superconducting properties of coated conductors irradiated with  $\text{He}^+$  ions at low temperature are substantially recovered by annealing at room temperature<sup>64</sup>.

## Conclusions

Understanding the tolerance of technological high temperature superconductors to fast neutron irradiation is crucial for the design of the next generation of compact fusion tokamaks. Ion irradiation is commonly used as a proxy for neutron damage owing to the experimental difficulties and huge expense associated with studying neutron irradiated samples. However, although many of the effects of neutron irradiation on the superconducting properties can be reproduced using ions, it is still unclear whether the damage mechanisms are the same. This is mainly because the point defects responsible are very difficult to

image in the TEM. In this study, we have used high energy resolution X-ray spectroscopy at the Cu K-edge combined with DFT modelling of defect structures, and XRD and TEM data to establish crystallographic data to calibrate the models, to gain new understanding of the nature of defects induced by  $\text{He}^+$  ion irradiation. In particular, we have found clear evidence that defects occur in the copper-oxygen planes, challenging the previous assumption in some of the literature that the decrease in  $T_c$  arises solely from loss of oxygen or oxygen disorder in the chains. Since the Cu-O planes are responsible for superconductivity, defects around the Cu(2) sites are expected to have a major impact on the superconducting transition temperature. We have found that the presence of Frenkel defects consisting of oxygen vacancies at the O(2) site in the plane and oxygen interstitials in between the Cu(2) and Cu(3) planes, which are known to be relatively low energy defects, reproduce many of the spectral and crystallographic changes observed as a result of ion irradiation. However, a more comprehensive study of a wider range of possible defect structures is required to support the conclusion that this is the most prevalent defect caused by ion irradiation.

This study provides the foundations for future research on the effect of different projectiles, including fast neutrons, on the nature of radiation damage. Since neutron experiments are highly expensive and restrictive, and fusion spectrum neutrons are not available at all, this detailed understanding of radiation damage mechanisms will allow the best proxies for neutron irradiation to be devised. In addition, our XANES and XRD results show that post-irradiation annealing results in a slight recovery of the material as the defect density decreases. This suggests that diffusional recovery mechanisms are important in determining the extent of radiation damage in REBCO, highlighting the acute need to assess radiation damage and recovery at the cryogenic temperatures relevant for the operation of fusion magnets.

## Methods

**Sample preparation.** We have used (Y,Gd)BCO-based 4 mm wide coated conductor with a 1  $\mu\text{m}$  thick superconducting layer manufactured by SuperPower in 2011 on a 50  $\mu\text{m}$  C276 Hastelloy substrate. The sequence of buffer layers, from substrate to REBCO layer, are alumina, yttria, magnesium oxide (textured using ion-beam assisted deposition (IBAD)) and lanthanum manganese oxide. After deposition of the (Y,Gd)BCO superconducting layer using metal-organic chemical vapour deposition (MOCVD), the coated conductor was encased in 2  $\mu\text{m}$  of silver and 20  $\mu\text{m}$  of copper<sup>45</sup>. To expose the REBCO layer, wet etching was used to remove the copper and silver outer layers. The copper layer was removed using a  $\text{FeCl}_3$  solution (60 g  $\text{FeCl}_3$  to 100 ml water) and the resultant silver chloride and underlying silver layers were subsequently removed with a mixture of ammonia and hydrogen peroxide (each 30% water solutions, mixed in 1:1 ratio)<sup>65</sup>. Disk samples were then produced using a 3 mm diameter TEM punch ensuring the exposed HTS is adjacent to the die during punching to minimise damage.

Annealing of the coated conductors was carried out using the conditions reported by Eley et al.<sup>66</sup>. Argon annealing was performed by encapsulating each disk sample in 1 atm argon within separate glass tubes. Each tube was then heated to 300 °C at 20 °C  $\text{min}^{-1}$  for 3 h. Each glass tube remained intact until mounting for the XANES experiment. Oxygen annealing was performed in flowing oxygen in a tube furnace at 300 °C for 3 h.

**Ion irradiation.** Irradiation of the samples with 300 keV helium was analysed using SRIM<sup>67</sup> to assess the level of damage and helium ion implantation. A full cascade calculation was performed using threshold displacement energies ( $E_d$ ) based on MacFarlane et al.<sup>57</sup> ( $E_d(\text{Gd}) = E_d(\text{Y}) = E_d(\text{Ba}) = E_d(\text{O}) = E_d(\text{Ni}) = 25$  eV;  $E_d(\text{Cu}) = 40$  eV) and lattice binding energy and surface binding energy set to 0 eV. The number of ions simulated was  $1 \times 10^5$ . Mass density of (Y,Gd)BCO was taken to be 6.632 g  $\text{cm}^{-3}$ , equivalent to a number density of  $7.455 \times 10^{22}$   $\text{cm}^{-3}$ . The hastelloy substrate was assumed to be 100% nickel of density 8.895 g  $\text{cm}^{-3}$ , equivalent to a number density of  $9.13 \times 10^{22}$   $\text{cm}^{-3}$ .

**Sample characterisation.** A  $T_c$  measurement of each disk sample was performed using a VSM insert in a Quantum Design MPMS3. Samples were placed between quartz blocks in the brass holder and zero field cooled to 20 K. The magnetic moment of the sample was measured on warming using a 5 mT measurement field.  $T_{c,\text{onset}}$  and  $T_{c,\text{offset}}$  values were defined as the intersection points of linear fits of the transition region with the normal state region just above  $T_c$  and the

superconducting region below  $T_c$ , respectively. The transition width was defined as  $\Delta T_c = T_{c,\text{onset}} - T_{c,\text{offset}}$ .

X-ray diffraction analysis was carried out in Bragg-Brentano geometry in a Panalytical Empyrean diffractometer using Cu K $\alpha$  X-rays. Highscore software was used to fit the background and the diffraction peaks and strip the K $\alpha_2$  component. Accurate  $c$ -axis lattice parameters were extracted by extrapolating to zero a plot of  $c$ -axis lattice parameter calculated from each (00l) peak against  $\frac{\cos^2\theta}{\sin\theta}$ , to correct for systematic errors arising from displacement of the sample surface from the diffractometer axis<sup>68</sup>. Williamson-Hall analysis was performed to estimate inhomogeneous strain in the sample<sup>68</sup>.

**STEM experiments.** TEM cross-sections from both the un-irradiated and irradiated samples were prepared by in-situ lift-out using focused ion beam milling in a ZEISS NVision 40 dual beam FIB using 30 kV Ga $^+$  ions down to a thickness of about 150 nm and final low energy surface cleaning using 2 kV 250 pA Ga $^+$  ions down to about 40 nm with a deliberate wedge shape of the lamella to ensure the ideal thickness for observing microstructural damage somewhere in the sample. Scanning Transmission Electron Microscopy (STEM) measurements were conducted on a JEOL ARM300F probe aberration-corrected microscope (at ePSIC-Diamond Light Source) operated at 300 kV accelerating voltage. We used a probe with 26.7 mrad convergence semi-angle and 25 pA current. High-angle annular dark-field STEM images were gathered at 9 cm camera length, with scattering collection angles of 77–210 mrad in the inner and outer range of the annular detector, respectively. For a more accurate atomic position measurements, we collected 10 HAADF frames, each 512 by 512 pixels, with scan dwell time of 5  $\mu$ sec [Using a plug-in developed by Bernhard Schaffer ([http://digitalmicrograph-scripting.tavernmaker.de/other%20packages/StackBuilder%20\(on%20image%20update\)%20tool.pdf](http://digitalmicrograph-scripting.tavernmaker.de/other%20packages/StackBuilder%20(on%20image%20update)%20tool.pdf))]. These stacks were aligned using hyperspy. Structural parameters were extracted from the aligned HAADF image stacks using the Atomap package to fit the Ba and RE (brightest) atomic column positions using centre of mass refinement first, and then 2D-Gaussian refinement<sup>50</sup>. Post-analysis to divide the data into the two different Ba sites and the RE site was performed using bespoke python code and the unit cell dimensions for about 300 unit cells per image stack were extracted from adjacent RE atom positions (see Supplementary Note 2).

**XAS experiments.** The HERFD-XAS experiments were performed at room temperature at beamline I20-Scanning<sup>69</sup> at Diamond Light Source (Didcot, United Kingdom). At the time of the measurements the synchrotron was operating with a ring energy of 3 GeV and at a current of 300 mA. The beamline was equipped with an in-house designed four-bounce scanning Si(111) monochromator<sup>70</sup> and the rejection of higher harmonics was achieved by using two dedicated Rh-coated mirrors operating at 4.5 mrad incidence angle. The x-ray emission spectrometer<sup>71</sup> based on a 1 m diameter Rowland circle operating in the Johann configuration in the vertical plane<sup>72</sup> was used for the experiment. The Cu K $\alpha_1$  emission line (8048 eV) was collected using three 100 mm diameter Si(444) spherically bent analyser crystals. An ionisation chamber filled with the appropriate mixture of He and Ar gases to absorb 20% of the beam was used as an incident intensity monitor, while a four element Medipix-Merlin photon-counting pixel detector<sup>73</sup> was used to monitor the K $\alpha_1$  emission line. All the HERFD-XANES measurements were collected at the peak of the K $\alpha_1$  line emission line. The total energy resolution is given by the convolution of the incident energy and the resolution provided by the spectrometer, and it is below 1 eV (~0.8 eV). The experimental spectra have been normalised to a step edge of 1, using the standard procedure<sup>74–77</sup>. Difference plots have been calculated from the normalised spectra. The energy calibration has been performed by setting zero energy to the first peak in the first derivative of the spectrum from the Cu foil standard, following the method in Heald et al.<sup>12</sup>.

**DFT calculations.** First principles simulations have been carried out using plane-wave pseudopotential density functional theory code CASTEP<sup>78</sup> together with the OptaDOS spectral simulation code<sup>79</sup> to simulate XANES spectra. The rSCAN functional<sup>80</sup> was used along with ultrasoft pseudopotentials. A cut-off energy of 650 eV and k-point spacing of 0.03 Å $^{-1}$  were used for the geometry optimisations, and all the structures were optimised until the forces on each atom were less than  $5 \times 10^{-3}$  eV Å $^{-1}$ . During the geometry optimisations, the structures were constrained to keep angles  $\alpha$ ,  $\beta$  and  $\gamma$  equal to 90°. The  $a$ ,  $b$  and  $c$  lattice parameters were allowed to change, and the atoms move, except in the case of the O(1) vacancy mode where the  $a$  and  $b$  lattice parameters were constrained to be the same. A cut-off energy of 650 eV and spectral k-point spacing of 0.02 Å $^{-1}$  were used for the XANES spectrum simulations. For both the geometry optimised and spectral calculation, increasing the cut-off energy and k-point spacing was found to have no visible effect on the simulated spectra.

To model the XANES spectra, a corehole has been created by removing a electron from the Cu 1s orbital. 2x2x1 supercells have been used for the XANES spectra simulations to prevent corehole-corehole interactions. Increasing the supercell size did not have any visual effect on the spectrum apart from the pre-edge region, which we have not considered in this paper. In order to compare the simulated spectra with experimental data, broadening due to instrumentation effects and life-time and been included in the calculation. The theoretical spectrum

was convolved with a Gaussian with a full width at half maximum (FWHM) of 1.0 eV to represent the energy resolution of the experimental set up. An energy dependent Lorentzian with a FWHM of E/10 eV, where E is the energy above the Fermi level, has been used to represent the broadening due to the finite lifetimes of the final states. Spectra were simulated for inequivalent sites and combined using the method of Mizoguchi et al.<sup>81</sup>. Charge density distributions were obtained from the DFT calculations using the c2x program<sup>82</sup>.

## Data availability

The data sets generated during this study are available from the ORA repository, [www.ora.ox.ac.uk](http://www.ora.ox.ac.uk), <https://doi.org/10.5287/bodleian:Mz7M9Q8aj>.

Received: 22 November 2021; Accepted: 11 July 2022;

Published online: 05 August 2022

## References

1. Sorbom, B. et al. Arc: a compact, high-field, fusion nuclear science facility and demonstration power plant with demountable magnets. *Fusion Eng. Des.* **100**, 378–405 (2015).
2. Braccini, V. et al. Properties of recent IBAD–MOCVD coated conductors relevant to their high field, low temperature magnet use. *Supercond. Sci. Technol.* **24**, 035001 (2010).
3. Umezawa, A. et al. Enhanced critical magnetization currents due to fast neutron irradiation in single-crystal  $\text{YBa}_2\text{Cu}_3\text{O}_{7-\delta}$ . *Phys. Rev. B* **36**, 7151–7154 (1987).
4. Sauerzopf, F. M. et al. Neutron-irradiation effects on critical current densities in single-crystalline  $\text{YBa}_2\text{Cu}_3\text{O}_{7-\delta}$ . *Phys. Rev. B* **43**, 3091–3100 (1991).
5. Sauerzopf, F. et al. Fast neutron irradiation and flux pinning in single crystalline high temperature superconductors. *Cryogenics* **33**, 8–13 (1993). *Critical Currents in high Tc superconductors*.
6. Sauerzopf, F. M., Wiesinger, H. P., Weber, H. W. & Crabtree, G. W. Analysis of pinning effects in  $\text{YBa}_2\text{Cu}_3\text{O}_{7-\delta}$  single crystals after fast neutron irradiation. *Phys. Rev. B* **51**, 6002–6012 (1995).
7. Eisterer, M., Fuger, R., Chudy, M., Hengstberger, F. & Weber, H. W. Neutron irradiation of coated conductors. *Supercond. Sci. Technol.* **23**, 014009 (2009).
8. Prokopec, R., Fischer, D. X., Weber, H. W. & Eisterer, M. Suitability of coated conductors for fusion magnets in view of their radiation response. *Supercond. Sci. Technol.* **28**, 014005 (2014).
9. Jirsa, M. et al. Electric currents in REBaCuO superconducting tapes. *Supercond. Sci. Technol.* **30**, 045010 (2017).
10. Fischer, D. X., Prokopec, R., Emhofer, J. & Eisterer, M. The effect of fast neutron irradiation on the superconducting properties of REBCO coated conductors with and without artificial pinning centers. *Supercond. Sci. Technol.* **31**, 044006 (2018).
11. LePage, Y. et al. Room-temperature structure of the 90-K bulk superconductor  $\text{YBa}_2\text{Cu}_3\text{O}_{8-x}$ . *Phys. Rev. B* **35**, 7245–7248 (1987).
12. Heald, S. M., Tranquada, J. M., Moodenbaugh, A. R. & Xu, Y. Orientation-dependent X-ray-absorption near-edge studies of high- $T_c$  superconductors. *Phys. Rev. B* **38**, 761–764 (1988).
13. Tranquada, J. M., Heald, S. M., Moodenbaugh, A. R. & Xu, Y. Mixed valency, hole concentration, and  $T_c$  in  $\text{YBa}_2\text{Cu}_3\text{O}_{6+x}$ . *Phys. Rev. B* **38**, 8893–8899 (1988).
14. Santoro, A. et al. The structure and properties of  $\text{Ba}_2\text{YCu}_3\text{O}_6$ . *Mater. Res. Bull.* **22**, 1007–1013 (1987).
15. Kirk, M. Structure and flux pinning properties of irradiation defects in  $\text{YBa}_2\text{Cu}_3\text{O}_{7-x}$ . *Cryogenics* **33**, 235–242 (1993). *Critical Currents in High Tc Superconductors*.
16. Aleksić, M. et al. Tem observation of neutron-induced collision cascades in Bi-2212 single crystals. *Phys. C Supercond.* **297**, 171–175 (1998).
17. Frischherz, M. C., Kirk, M. A., Zhang, J. P. & Weber, H. W. Transmission electron microscopy of defect cascades in  $\text{YBa}_2\text{Cu}_3\text{O}_{7-\delta}$  produced by ion irradiation. *Philos. Mag. A* **67**, 1347–1363 (1993).
18. Sauerzopf, F. M. Anisotropic flux pinning in  $\text{YBa}_2\text{Cu}_3\text{O}_{7-\delta}$  single crystals: the influence of defect size and density as determined from neutron irradiation. *Phys. Rev. B* **57**, 10959–10971 (1998).
19. Müller, B. et al. Josephson junctions and squids created by focused helium-ion-beam irradiation of  $\text{YBa}_2\text{Cu}_3\text{O}_7$ . *Phys. Rev. Appl.* **11**, 044082 (2019).
20. Cybart, S. et al. Nano josephson superconducting tunnel junctions in  $\text{YBa}_2\text{Cu}_3\text{O}_{7-\delta}$  directly patterned with a focused helium ion beam. *Nat. Nano* **10**, 598 (2015).
21. Cho, E. et al.  $\text{YBa}_2\text{Cu}_3\text{O}_{7-\delta}$  superconducting quantum interference devices with metal-lic to insulating barriers written with a focused helium ion beam. *Appl. Phys. Lett.* **106**, 252601 (2015).

22. Sefrioui, Z. et al. Vortex liquid entanglement in irradiated  $\text{YBa}_2\text{Cu}_3\text{O}_7$  thin films. *Phys. Rev. B* **63**, 064503 (2001).

23. Navacerrada, M. A. et al. Critical temperature depression and persistent photoconductivity in ion irradiated  $\text{YBa}_2\text{Cu}_3\text{O}_{7-x}$  films and  $\text{YBa}_2\text{Cu}_3\text{O}_{7-x}/\text{PrBa}_2\text{Cu}_3\text{O}_7$  superlattices. *Appl. Phys. Lett.* **76**, 3289–3291 (2000).

24. Meyer, O. et al. Transport and structure of ion irradiated htsc thin films. *Nucl. Instrum. Methods Phys. Res. Sect. B* **65**, 539–545 (1992).

25. Hensel, B. et al. Ion irradiation of epitaxial  $\text{YBa}_2\text{Cu}_3\text{O}_{7-\delta}$  films: effects of electronic energy loss. *Phys. Rev. B* **42**, 4135–4142 (1990).

26. Xiong, G. C., Li, H. C., Linker, G. & Meyer, O. Transport properties, phase transition, and recovery near 200 K of proton-irradiated  $\text{YBa}_2\text{Cu}_3\text{O}_7$  thin films. *Phys. Rev. B* **38**, 240–243 (1988).

27. Civale, L. et al. Defect independence of the irreversibility line in proton-irradiated Y-Ba-Cu-O crystals. *Phys. Rev. Lett.* **65**, 1164–1167 (1990).

28. van Dover, R. B. et al. Critical currents in proton-irradiated single-crystal  $\text{Ba}_2\text{YCu}_3\text{O}_{7-\delta}$ . *Appl. Phys. Lett.* **56**, 2681–2683 (1990).

29. Valles, J. M. et al. Ion-beam-induced metal-insulator transition in  $\text{YBa}_2\text{Cu}_3\text{O}_{7-\delta}$ : a mobility edge. *Phys. Rev. B* **39**, 11599–11602 (1989).

30. Menushenkov, A. et al. Polarized XAS spectroscopy of HTSC thin films. *Nucl. Instrum. Methods Phys. Res. Sect. A* **359**, 236–239 (1995). Proceedings of the 10th National Synchrotron Radiation Conference.

31. Giapintzakis, J., Ginsberg, D., Kirk, M. & Ockers, S. Testing models of the symmetry of the superconducting pairing state by low-temperature electron irradiation of an untwinned single crystal of  $\text{YBa}_2\text{Cu}_3\text{O}_7$ . *Phys. Rev. B* **50**, 15967 (1994).

32. Zhang, Y., Rupich, M., Solovyov, V., Qiang, L. & Goyal, A. Dynamic behavior of reversible oxygen migration in irradiated-annealed high temperature superconducting wires. *Sci. Rep.* **10**, 14848 (2020).

33. Bianconi, A. et al. Lack of delocalized cup states at the fermi level in the high- $T_c$  superconductor  $\text{YBa}_2\text{Cu}_3\text{O}_7$  by xanes spectroscopy. *Zeitschrift für Physik B Condensed Matter* **67**, 307–312 (1987).

34. Antonini, G. M., Calandra, C., Corni, F., Matacotta, F. C. & Sacchi, M. Atomic local coordinations and multivalent states in  $\text{YBa}_2\text{Cu}_3\text{O}_{9-\delta}$  superconductors. *Europhys. Lett.* **4**, 851–856 (1987).

35. Lytle, F. W., Gregor, R. B. & Panson, A. J. Discussion of X-ray-absorption near-edge structure: application to Cu in the high- $T_c$  superconductors  $\text{La}_{1.8}\text{Sr}_0.2\text{CuO}_4$  and  $\text{YBa}_2\text{Cu}_3\text{O}_7$ . *Phys. Rev. B* **37**, 1550–1562 (1988).

36. Hämäläinen, K., Siddons, D. P., Hastings, J. B. & Berman, L. E. Elimination of the inner-shell lifetime broadening in X-ray-absorption spectroscopy. *Phys. Rev. Lett.* **67**, 2850–2853 (1991).

37. Agote-Aráñ, M. et al. Operando HERFD-XANES/XES studies reveal differences in the activity of Fe-species in MFI and CHA structures for the standard selective catalytic reduction of NO with NH<sub>3</sub>. *Appl. Catal. A* **570**, 283–291 (2019).

38. Celorio, V. et al. Relationship between mn oxidation state changes and oxygen reduction activity in  $(\text{La,Ca})\text{MnO}_3$  as probed by in situ xas and xes. *ACS Catal.* **11**, 6431–6439 (2021).

39. Cui, Y.-T. et al. Wetting induced oxidation of pt-based nano catalysts revealed by in situ high energy resolution x-ray absorption spectroscopy. *Sci. Rep.* **7**, 1482 (2017).

40. Butorin, S. M., Kvashnina, K. O., Vegelius, J. R., Meyer, D. & Shuh, D. K. High-resolution X-ray absorption spectroscopy as a probe of crystal-field and covalency effects in actinide compounds. *Proc. Natl Acad. Sci.* **113**, 8093–8097 (2016).

41. Cutsail, G. E. et al. High-resolution iron X-ray absorption spectroscopic and computational studies of non-heme diiron peroxy intermediates. *J. Inorg. Biochem.* **203**, 110877 (2020).

42. Björnsson, R. et al. Identification of a spin-coupled Mo(III) in the nitrogenase iron-molybdenum cofactor. *Chem. Sci.* **5**, 3096–3103 (2014).

43. Huzan, M. S. et al. Single-ion magnetism in the extended solid-state: insights from X-ray absorption and emission spectroscopy. *Chem. Sci.* **11**, 11801–11810 (2020).

44. Arias-Egido, E. et al. Dimensionality-driven metal-insulator transition in spin-orbit-coupled  $\text{IrO}_2$ . *Nanoscale* <https://doi.org/10.1039/D1NR04207F> (2021).

45. Sundaram, A. et al. 2G HTS wires made on 30  $\mu\text{m}$  thick hastelloy substrate. *Supercond. Sci. Technol.* **29**, 104007 (2016).

46. Wen, S., Song, X. & Feng, J. Some microstructure features in  $\text{RBA}_2\text{Cu}_3\text{O}_{7-x}$  ceramics. *Mater. Lett.* **6**, 385 (1988).

47. Ferrando, V. et al. Systematic study of disorder induced by neutron irradiation in  $\text{MgB}_2$  thin films. *J. Appl. Phys.* **101**, 043903 (2007).

48. Poate, J. M., Dynes, R. C., Testardi, L. R. & Hammond, R. H. Comments on defect production and stoichiometry in  $A-15$  superconductors. *Phys. Rev. Lett.* **37**, 1308–1311 (1976).

49. Benzi, P., Bottizzo, E. & Rizza, N. Oxygen determination from cell dimensions in YBCO superconductors. *J. Cryst. Growth* **269**, 625 (2004).

50. Nord, M., Vullum, P., MacLaren, I., Tybrell, T. & Holmestad, R. Atomap: a new software tool for the automated analysis of atomic resolution images using two-dimensional gaussian fitting. *Adv. Struct. Chem. Imag.* **3**, 9 (2017).

51. Baker, M. L. et al. K- and L-edge X-ray absorption spectroscopy (XAS) and resonant inelastic X-ray scattering (RIXS) determination of differential orbital covalency (DOC) of transition metal sites. *Coordination Chem. Rev.* **345**, 182–208 (2017).

52. Kosugi, N., Kondoh, H., Tajima, H. & Kuroda, H. Cu K-edge XANES of  $(\text{La}_{1-x}\text{Sr}_x)_2\text{CuO}_4$ ,  $\text{YBa}_2\text{Cu}_3\text{O}_y$  and related Cu oxides. valence, structure and final-state effects on 1s-4pII and 1s-4p $\sigma$  absorption. *Chem. Phys.* **135**, 149–160 (1989).

53. Garg, K., Bianconi, A., Della Longa, S., Clozza, A. & De Santis, M. Multiple-scattering analysis of K-edge X-ray-absorption near-edge spectrum of  $\text{YBa}_2\text{Cu}_3\text{O}_7$ . *Phys. Rev. B* **38**, 244–251 (1988).

54. Singh, B. N. & Zinkle, S. J. Defect accumulation in pure FCC metals in the transient regime: a review. *J. Nucl. Mater.* **206**, 212 (1993).

55. Nordlund, K. Historical review of computer simulation of radiation effects in materials. *J. Nucl. Mater.* **520**, 273 (2019).

56. Stoneham, A. & Smith, L. Defect phenomena in superconducting oxides and analogous ceramic oxides. *J. Phys. Condens. Matter* **3**, 225 (1991).

57. MacFarlane, R. & Kahler, A. Methods for processing ENDF/B-VII with NJOY. *Nucl. Data Sheets* **111**, 2739 (2010).

58. Legris, A., Rullier-Albenque, F., Radeva, E. & P., L. Effects of electron irradiation on  $\text{YBa}_2\text{Cu}_3\text{O}_7$ . *J. Phys. I. France* **3**, 1605 (1993).

59. Tolpygo, S., Lin, J.-Y., Gurvitch, M., Hou, S. & Phillips, J. Displacement energy for plane and chain oxygen and implications for irradiation-induced resistivity and  $T_c$  suppression. *Phys. Rev. B* **53**, 12462 (1996).

60. Islam, M. Computer simulation study of oxygen migration in  $\text{YBa}_2\text{Cu}_3\text{O}_7$ . *Supercond. Sci. Technol.* **3**, 531636 (1990).

61. Murphy, S. A point defect model for  $\text{YBa}_2\text{Cu}_3\text{O}_7$  from density functional theory. *J. Phys. Commun.* **4**, 115003 (2020).

62. Horide, T. & Matsumoto, K. Anisotropic strain dependence of oxygen vacancy formation in  $\text{YBa}_2\text{Cu}_3\text{O}_{7-\delta}$ : first principle study. *Supercond. Sci. Technol.* **27**, 115013 (2014).

63. Gray, R. L., Rushton, M. J. D. & Murphy, S. T. Molecular dynamics simulations of radiation damage in  $\text{YBa}_2\text{Cu}_3\text{O}_7$ . *Supercond. Sci. Technol.* **35**, 035010 (2022).

64. Iliffe, W. et al. In-situ measurements of the effect of radiation damage on the superconducting properties of coated conductors. *Supercond. Sci. Technol.* **34**, 09LT01 (2021).

65. Brittles, G. D., Mousavi, T., Grovenor, C. R. M., Aksoy, C. & Speller, S. C. Persistent current joints between technological superconductors. *Supercond. Sci. Technol.* **28**, 093001 (2015).

66. Eley, S. et al. Decoupling and tuning competing effects of different types of defects on flux creep in irradiated  $\text{YBa}_2\text{Cu}_3\text{O}_{7-\delta}$  coated conductors. *Supercond. Sci. Technol.* **30**, 015010 (2017).

67. Ziegler, F., Ziegler, M. & Biersack, J. Srim - the stopping and range of ions in matter. *Nucl. Instrum. Methods Phys. Res. Sect. B* **268**, 1818 (2010).

68. Suryanarayana, C. & Grant Norton, M. *X-ray diffraction: a practical approach* (Springer, 1998).

69. Diaz-Moreno, S. et al. The spectroscopy village at diamond light source. *J. Synchrotron Radiat.* **25**, 998–1009 (2018).

70. Hayama, S. et al. The scanning four-bounce monochromator for beamline I20 at the Diamond Light Source. *J. Synchrotron Radiation* **25**, 1556–1564 (2018).

71. Hayama, S. et al. Photon-in/photon-out spectroscopy at the I20-scanning beamline at diamond light source. *J. Phys. Condens. Matter* **33**, 284003 (2021).

72. Johann, H. Die erzeugung lichtstarker röntgenspektren mit hilfe von konkavkristallen. *Zeitschrift Für Physik* **69**, 185–206 (1931).

73. Plackett, R. et al. Merlin: a fast versatile readout system for Medipix3. *JINST* **8**, C01038–C01038 (2013).

74. Konigsberger, D. & Prins, R. *X-ray absorption: principles, applications, techniques of EXAFS, SEXAFS, and XANES* (John Wiley and Sons, 1988).

75. Stern, E., Heald, S. & Koch, E. Principles and applications of EXAFS, Chapter 10. In *Handbook of synchrotron radiation* (North-Holland, 1983).

76. Penner-Hahn, J. X-ray absorption spectroscopy in coordination chemistry. *Coordination Chem. Rev.* **190–192**, 1101–1123 (1999).

77. Penner-Hahn, J. X-ray absorption spectroscopy. In *Comprehensive Coordination Chemistry II*, 159–286 (Elsevier, 2003).

78. Clark, S. J. et al. First principles methods using CASTEP. *Z. Kristall.* **220**, 567–570 (2005).

79. Morris, A. J., Nicholls, R. J., Pickard, C. J. & Yates, J. R. Optados: a tool for obtaining density of states, core-level and optical spectra from electronic structure codes. *Comput. Phys. Commun.* **185**, 1477–1485 (2014).

80. Bartók, A. & Yates, J. Regularized SCAN functional. *J. Chem. Phys.* **150**, 161101 (2019).

81. Mizoguchi, T., Tanaka, I., Gao, S.-P. & Pickard, C. J. First-principles calculation of spectral features, chemical shift and absolute threshold of ELNES and XANES using a plane wave pseudopotential method. *J. Phys. Condens. Matter.* **21**, 104204 (2009).

82. Rutter, M. C2x: a tool for visualisation and input preparation for CASTEP and other electronic structure codes. *Comput. Phys. Commun.* **225**, 174–179 (2018).

83. Schweiss, P. et al. Static and dynamic displacements in R  $\text{Ba}_2 \text{Cu}_3 \text{O}_{7-\delta}$  ( $\text{R}=\text{Y, ho}$ ;  $\delta=0.05, 0.5$ ). *Phys. Rev. B* **49**, 1387–1396 (1994).
84. Fernandes, A. A. R. et al. Effect of physical and chemical pressure on the superconductivity of high-temperature oxide superconductors. *Phys. Rev. B* **44**, 7601–7606 (1991).

## Acknowledgements

We acknowledge Diamond Light Source for time on Beamline I20 under Proposals SP23408, SP27236 and SP28846 and time at ePSIC on E02 under proposal MG28480. We also acknowledge the David Cockayne Centre for Electron Microscopy for access to sample preparation facilities and Surrey Ion Beam centre for the  $\text{He}^+$  ion irradiation. R.J.N. gratefully acknowledges financial support from the EPSRC, grant EP/L022907/1.

## Author contributions

S.C.S. and R.J.N. conceived and guided the research. S.D.-M. and M.A. designed the HERFD-XAS experiment and helped with data analysis. W.I. prepared the samples for HERFD-XAS and performed the superconducting property measurements and SRIM analysis. Y.L. fabricated the thin foil STEM samples and was involved with the STEM data collection. M.D. operated the ARM TEM at ePSIC and helped with the STEM data analysis. R.J.N., S.D.-M., W.I., T.M., M.A., C.R.M.G. and S.C.S. were involved in the HERFD-XAS data collection. R.J.N. performed the DFT modelling. S.C.S. was responsible for the majority of the XANES and STEM analysis. C.R.M.G. led the STEM experiment. R.J.N. and S.C.S. draughted the manuscript and C.R.M.G. suggested manuscript revisions. All authors commented on the draughts.

## Competing interests

The authors declare no competing interests.

## Additional information

**Supplementary information** The online version contains supplementary material available at <https://doi.org/10.1038/s43246-022-00272-0>.

**Correspondence** and requests for materials should be addressed to Rebecca J. Nicholls or Susannah C. Speller.

**Peer review information** *Communications Materials* thanks Yuhu Zhai and the other, anonymous, reviewer(s) for their contribution to the peer review of this work. Primary Handling Editors: Nicola Poccia and Aldo Isidori.

**Reprints and permission information** is available at <http://www.nature.com/reprints>

**Publisher's note** Springer Nature remains neutral with regard to jurisdictional claims in published maps and institutional affiliations.



**Open Access** This article is licensed under a Creative Commons Attribution 4.0 International License, which permits use, sharing, adaptation, distribution and reproduction in any medium or format, as long as you give appropriate credit to the original author(s) and the source, provide a link to the Creative Commons license, and indicate if changes were made. The images or other third party material in this article are included in the article's Creative Commons license, unless indicated otherwise in a credit line to the material. If material is not included in the article's Creative Commons license and your intended use is not permitted by statutory regulation or exceeds the permitted use, you will need to obtain permission directly from the copyright holder. To view a copy of this license, visit <http://creativecommons.org/licenses/by/4.0/>.

© The Author(s) 2022